COMMUNICATION

Check for updates

Colloidal synthesis of lead-free Cs$_2$TiBr$_{6-x}$I$_x$ perovskite nanocrystals†

Shanti Maria Liga [a] and Gerasimos Konstantatos ⋆[ab]

Cesium titanium halide perovskites are novel lead-free optoelectronic materials that have attracted attention in the last two years for their application in solar cells with power conversion efficiencies reaching 3.3%. We report here the first colloidal synthesis of pure and mixed bromide–iodide cesium titanium perovskite nanocrystals with a bandgap tunable from 2.3 eV to 1.2 eV.

Since their first introduction in solar cells in 2009,[1] APbX$_3$ (where A = Cs$^+$, CH$_3$NH$_3^+$, CH(NH$_2$)$_2^+$; X = Cl$^-$, Br$^-$, I$^-$) perovskites have acquired a pivotal role as an emerging class of semiconductors, thanks to their remarkable optoelectronic properties[2–5] combined with the ease of solution processability. Their first synthesis as nanocrystals (NCs) dates back to 2015,[6] with their outstanding properties when applied in several devices, such as solar cells,[7–9] light emitting diodes,[10,11] photodetectors[12] and lasers,[13] being already documented. Despite the compelling performance achieved, the use of lead imposes regulatory and environmental concerns.[14] To tackle this problem, in recent years the computational research community has focused on the search for alternative elements to lead, with a focus on those that are not toxic and that can produce a stable perovskite structure.[15–17] Among them so far only Sn-based perovskites offer direct bandgaps with values useful for solar cell applications, yet suffering from the notorious oxidation of Sn^{2+}.

Vacancy-ordered halide perovskites are one of the alternative structures that have been designed to replace Pb^{2+} with tetravalent cations. They have the general formula A$_2$BX$_6$, which is obtained by the removal of half the B^{2+} cations in the archetypical ABX$_3$ perovskite structure, and the use of tetravalent cations instead in order to balance the charges (see Scheme 1). Over the last 5 years, vacancy-ordered perovskites containing

tin,[18,19] palladium,[20] tellurium,[21] zirconium[22] and titanium[23,24] have been synthesized and characterized. Among them, the cesium titanium halide perovskite stands out as a promising candidate for lead-free perovskite solar cells in view of its favorable bandgap for solar cell applications. Cs$_2$TiBr$_6$ solar cells have been reported with a power conversion efficiency (PCE) of 3.3%,[24] higher than what has been reached with double perovskites that have been studied for a longer time, such as tin vacancy-ordered perovskites, whose solar cells reached a maximum of 2.1% PCE,[25] or Cs$_2$AgBiBr$_6$, which has received great interest due to its stability and straightforward synthesis but whose bandgap is not optimal for solar harnessing, with the reported solar cells achieving a maximum PCE of 2.84%.[26]

To date, the Cs$_2$TiBr$_6$ perovskite has been synthesized with different methods, none of which is a low temperature and easily scalable solution method that leads to stock solutions suitable for making low-cost thin films for optoelectronic devices.[23,24,27] While Cs$_2$TiBr$_6$ with a bandgap of 1.8 eV has been grown via vapor deposition at high temperatures,[24] Cs$_2$TiBr$_{6-x}$I$_x$, which offers bandgap tunability down to 1.2 eV, has only been grown by melt-crystallization at high temperatures,[23] yielding crystal powders and preventing its application in devices.

A solution method has yet to be reported due to the difficulty in finding a solvent in which both CsBr/CsI and TiBr$_4$/TiI$_4$ are soluble, since cesium halides dissolve only in highly polar solvents while titanium halides react with them.

In this paper, we present a new approach for the synthesis of Cs$_2$TiBr$_6$ and mixed bromide/iodide Cs$_2$TiBr$_{6-x}$I$_x$ nanocrystals, which consists of performing a colloidal synthesis using the hot-injection method. With this method, we were able to synthesize stable solutions of mixed bromide/iodide Cs$_2$TiBr$_{6-x}$I$_x$ NCs that can be easily deposited as thin films. The Cs$_2$TiBr$_{6-x}$I$_x$ NCs have a bandgap tunable from 2.3 eV to 1.2 eV and the Cs$_2$TiBr$_6$ NC solution shows emission at 580 nm.
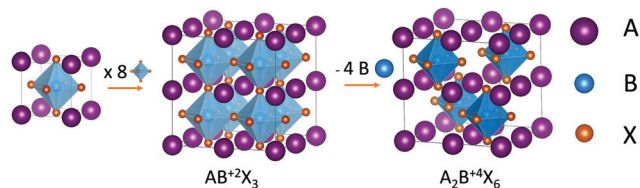
For the synthesis of Cs$_2$TiBr$_6$ NCs, cesium acetate and titanium oleate were loaded in a flask together with oleic acid, 3-(N,N-dimethyloctadecylammonio)propanesulfonate and octadecene. Bromotrimethylsilane (TMSBr) was swiftly injected at

[a] ICFO, Institut de Ciencies Fotoniques, The Barcelona Institute of Science and Technology, 08860 Castelldefels, Barcelona, Spain. E-mail: gerasimos.konstantatos@icfo.es

[b] ICREA, Institució Catalana de Recerca i Estudis Avançats, 08010 Barcelona, Spain
† Electronic supplementary information (ESI) available: Additional XRD data, TEM images with size distribution and symmetry analyses, STEM-EDS maps, Tauc plots of Cs$_2$TiBr$_{6-x}$I$_x$ NC solutions and pictures for visual comparisons of different treatments. See DOI: 10.1039/d1tc01732b

11098 | J. Mater. Chem. C, 2021, 9, 11098–11103

This journal is © The Royal Society of Chemistry 2021

Scheme 1 Relation between the structure of vacancy-ordered halide perovskites and the structure of the archetypical ABX_3 perovskite.
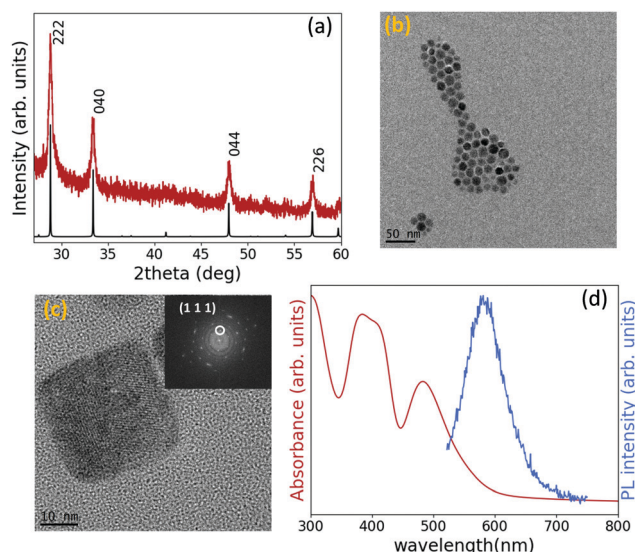
Fig. 1 (a) XRD pattern of Cs_2TiBr_6 NCs with the corresponding simulated reflections for Cs_2TiBr_6 with the same lattice parameter. (b) TEM image and (c) HRTEM image of Cs_2TiBr_6 NCs. In the inset of (c), the FFT of the image, from where the d-spacings were extracted. (d) Absorption and PL spectra of washed Cs_2TiBr_6 NCs diluted in toluene.

140 °C under argon and after a few seconds the reaction was quenched by diluting the nanocrystals in toluene while lowering the temperature. After the injection, the solution changed color from pale orange to dark red.

Fig. 1(a) shows the XRD pattern of the as-synthesized nanoparticles and the simulated XRD pattern of Cs_2TiBr_6, which indicates that the crystal possesses $Fm\bar{3}m$ space group symmetry. Using Bragg's law, a lattice constant of 10.72 Å was calculated, very close to the values reported in the literature for bulk Cs_2TiBr_6.[23,27,28] The optimized synthesis required a Cs/Ti/Br molar ratio of 2 : 2.5 : 13.5, otherwise a CsBr peak was detected in the XRD pattern (Fig. S1, ESI†). The XRD pattern of $TiBr_4$ powder was also measured to confirm it was not present in the NC solution as a byproduct (Fig. S2, ESI†). The structural characterization of the Cs_2TiBr_6 perovskite nanoparticles was completed carrying out a TEM analysis. Fig. 1(b) shows that the synthesis produces well-dispersed nanoparticles with a controlled size distribution, with an average diameter of 12.9 nm, a size deviation of ±1.7 nm and a symmetrical shape (Fig. S3, ESI†). Fig. 1(c) is a High Resolution TEM (HRTEM) image of the same sample from where d-spacings can be

calculated through a fast Fourier transform (FFT) of the image, represented in the inset of Fig. 1(c). The d-spacings calculated from the image match those ones obtained considering a lattice parameter of 10.72 Å, inferred from the XRD pattern. Moreover, STEM-EDS analysis performed on ensembles of NCs detected the presence of Cs, Ti and Br (Fig. S4, ESI†), and inductively coupled plasma optical emission spectroscopy (ICP-OES) results confirm that the ratio Cs/Ti is very close to 2, as expected from the stoichiometry (Table S1, ESI†). To investigate the optical properties of the Cs_2TiBr_6 colloidal solution, the absorption and emission of the washed solution were measured and are shown in Fig. 1(d). Taking into account the quasi-direct bandgap nature calculated for Cs_2TiBr_6,[24] the optical bandgap was extracted from the Tauc plots, considering both a direct and indirect bandgap, and it is equal to 2.3 eV and 2 eV, respectively (Fig. S5, ESI†), around 0.5 eV higher than the values reported for bulk Cs_2TiBr_6.[23,24,29] The absorption spectrum has the same shape observed for the bulk material, with two peaks at 390 nm and 483 nm representing the two parity-allowed transitions.[29] The emission peak falls at 580 nm (2.1 eV) and should represent a band-edge transition. The PLQY was measured at an excitation wavelength of 480 nm using Rhodamine 6G in absolute ethanol as a reference, and has a value far below 1%. Such a low value is consistent with the calculated parity-forbidden nature of the bandgap.[29]

The zwitterionic ligand, namely 3-(N,N-dimethyloctadecyl-ammonio)propanesulfonate, is used in the synthesis in order to stabilize the nanoparticles during the washing procedure, but it does not play a crucial role in controlling the shape of the nanoparticles. Indeed, in the first attempts to synthesize Cs_2TiBr_6 NCs, only oleic acid was used as a ligand and produced very similarly shaped nanoparticles with a homogeneous size distribution (Fig. S6, ESI†). However, the as-prepared nanoparticles were very sensitive to any antisolvent used during the washing. On the contrary, with the use of the zwitterionic ligand the nanoparticles are stabilized so that they can be precipitated with acetone and then easily redispersed in toluene. This ligand was preferred to the classically used long chain organic amines, for instance oleylamine or octylamine, because when using the latter XRD showed CsBr contamination and the dark red solution turned milky a few seconds after the reaction occurred. The production of CsBr as a byproduct and the change of color from dark red to milky diminish when the temperature of TMSBr injection is lowered or when the ligand is added after the synthesis at room temperature (Fig. S7, ESI†). To understand the reactivity of these amines with Cs_2TiBr_6, we mixed different ligands with a solution of $TiBr_4$ dissolved in toluene, and observed that amines with the lone pair in the nitrogen atom available reacted with $TiBr_4$ producing a white powder, while quaternary amines or organic acids did not produce any change in the color of the $TiBr_4$ solution (Fig. S8, ESI†). From these experimental observations, we hypothesized that the strong electrophilic nature of titanium in oxidation state +4 combined with the nucleophilicity of primary, secondary or ternary amines could give rise to adducts of amines and Ti(IV)Br_4, as already observed in the literature for the case of Ti(IV)Cl_4.[30] The zwitterionic ligand contains a quaternary aminic group, so that this possible secondary reaction is avoided; moreover,

This journal is © The Royal Society of Chemistry 2021

J. Mater. Chem. C, 2021, **9**, 11098–11103 | **11099**

this ligand was demonstrated to stabilize colloidal perovskite solutions better than the common oleic acid/oleylamine system.[31]

Lastly, it was observed that when the reaction is quenched with a water bath the nanocrystals grow with the irregular shape of big rods, both when using only oleic acid and when adding the zwitterionic ligand (Fig. S9, ESI†). Lowering the temperature without diluting the precursors is not effective in quenching the reaction because Cs_2TiBr_6 NCs are produced also at lower temperature (Fig. S10, ESI†) but they grow with less symmetrical shapes (Fig. S11, ESI†). On the contrary, diluting the solution with toluene quenches the reaction quickly because it decreases the temperature and dilutes the precursors simultaneously, preventing further growth of the NCs. With this method, only NCs grown at high temperature, which are the most symmetrical ones, are produced.

Once the synthesis of Cs_2TiBr_6 NCs was optimized, we used the same colloidal method to attempt the synthesis of pure Cs_2TiI_6 and mixed-halide $Cs_2TiBr_{6-x}I_x$ NCs, by partially or fully replacing TMSBr with TMSI. Fig. 2(a) illustrates the XRD patterns of pure bromide Cs_2TiBr_6, pure iodide Cs_2TiI_6 and of the mixed-halide species. All crystals possess $Fm\bar{3}m$ space group symmetry and, as expected, the diffraction angles decrease going from the pure bromide to the pure iodide perovskite, indicating an increase in the unit cell parameter from 10.72 Å to 11.5 Å for Cs_2TiI_6 (Fig. 2(b)). Using Vegard's law, we calculated the amount of iodide inserted for each different precursor ratio (Fig. S12, ESI†). The XRD pattern of TiI_4 powder confirms that TiI_4 was not present in the NC solution (Fig. S2, ESI†). TEM images of the mixed-halide perovskites and of the pure iodide perovskite illustrate that the synthesis produces polydisperse nanoparticles with less regular shapes than the

bromide NCs (Fig. 2(c) and Fig. S13, ESI†). A HRTEM image of the pure iodide Cs_2TiI_6 perovskite shows d-spacings matching the lattice parameter extracted from the XRD pattern (Fig. 2(d)). Additionally, STEM/EDS analysis of the pure iodide and mixed-halide samples confirmed the presence of Cs, Ti and both Br and I (Fig. S14 and S15, ESI†) and ICP-OES confirmed that the ratio of Cs and Ti in the structure is around 2 (Table S1, ESI†).

Fig. 3(a) shows the absorption spectra of the mixed-halide perovskite solutions. When increasing the amount of iodide in the structure, the absorption onset shifts towards longer wavelengths, and two characteristic peaks at around 570 nm and 790 nm appear. This redshift of the absorption onset is clearly visible already when just 24% of bromide has been replaced by iodide (Fig. 3(b)). The direct bandgaps for all the combinations were extracted from Tauc plots (Fig. S16, ESI†) and plotted against the ratio of iodide and bromide in the structure (Fig. 3(c)). It is possible to tune the bandgap from 2.3 eV to 1.2 eV when 87% of bromide has been replaced by iodide. The bandgap decreases until 87% replacement but then increases to 1.3 eV for the pure iodide perovskite. This trend is in agreement with previously reported theoretical values,[23] plotted in Fig. 3(c), and is ascribed likely to bandgap reduction from Urbach tailing due to anionic disorder in the crystal structure.

In the literature there are contradictory results about the stability of Cs_2TiBr_6 in air. Some studies claim that this material is intrinsically and environmentally stable,[23,24,27] while others found that it decomposes quickly in air, producing CsBr and amorphous titanium oxide.[29,32] The colloidal Cs_2TiBr_6 NC solution and films prepared by dropcasting the solution on silicon or glass substrates are stable for weeks when prepared and stored under a nitrogen atmosphere. However, we
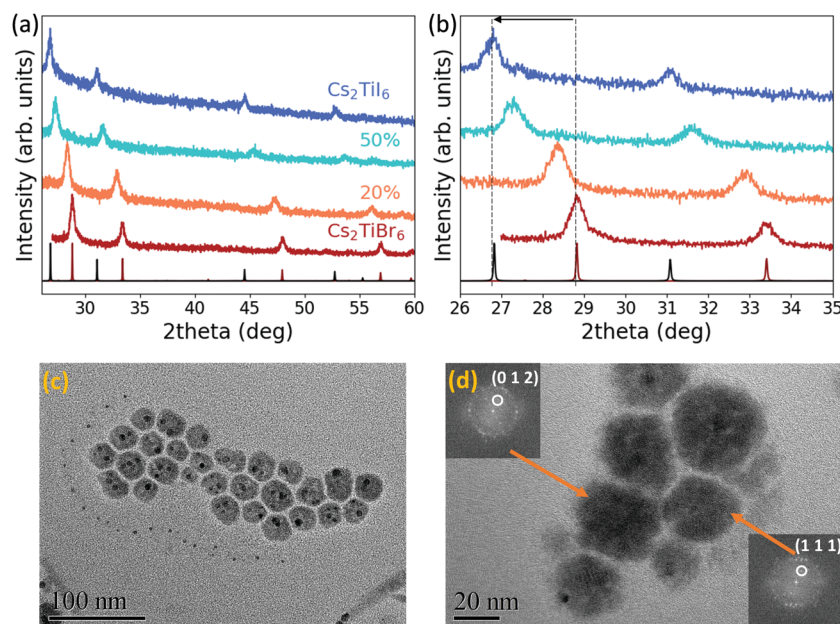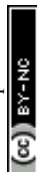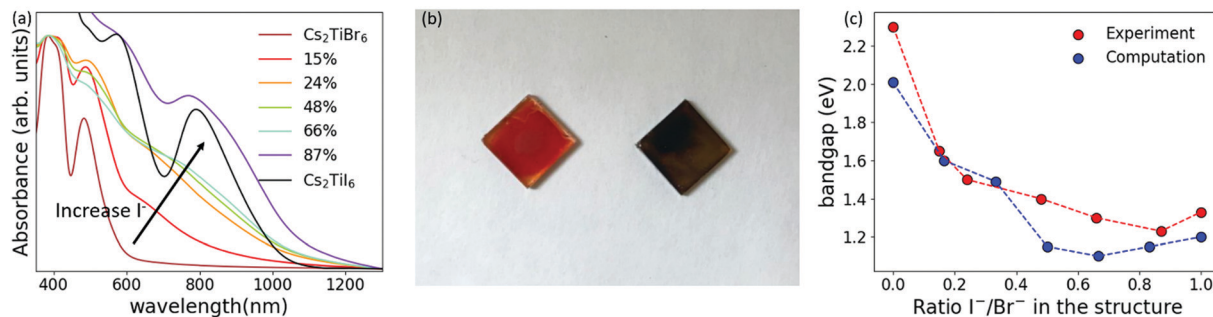

Fig. 2 (a) XRD patterns of mixed halide $Cs_2TiBr_{6-x}I_x$ NCs with the corresponding standards of pure bromide (bordeaux) and pure iodide (black) perovskites. (b) Expanded XRD pattern. (c) TEM image of $Cs_2TiBr_{6-x}I_x$ NCs prepared using TMSI and TMSBr in ratio 0.7. (d) HRTEM image of Cs_2TiI_6 NCs. In the two insets of (d), FFT images of the two NCs.

11100 | J. Mater. Chem. C, 2021, 9, 11098–11103

This journal is © The Royal Society of Chemistry 2021

Fig. 3 (a) Absorption spectra of $Cs_2TiBr_{6-x}I_x$ NCs. (b) Picture of Cs_2TiBr_6 and $Cs_2TiBr_{4.5}I_{1.5}$ films prepared from the colloidal solutions. (c) Comparison between experimental bandgaps and computed bandgaps of a series of $Cs_2TiBr_{6-x}I_x$ perovskites. The theoretically predicted values were taken from the literature.

observed fast degradation of the films into CsBr when exposing them to air (Fig. S17 and S18, ESI†). Such fast decomposition probably occurs because the nanoparticles have a much bigger surface to volume ratio compared to the bulk, and therefore are more susceptible to decomposition due to the interaction with humidity and oxygen. To further investigate the stability of the Cs_2TiBr_6 NC films under environmental conditions, we exposed them to UV-light and heat under a nitrogen atmosphere. The NC films are stable after 4 hours under UV light at 395 nm with a power density of 15 mW m^{-2}, and for 1 hour at 100 °C (Fig. S18, ESI†). We heated the films for 1 hour at increasing temperatures and observed partial degradation at 150 °C, and complete degradation into CsBr and most probably into amorphous titanium oxide at 300 °C (Fig. S19, ESI†).

Conclusions

In summary, we have reported the first colloidal route to synthesize Cs_2TiBr_6 vacancy-ordered perovskite NCs with good control over their size distribution and shape, a bandgap of 2.3 eV and an emission peak at 580 nm. Moreover, we demonstrated that by partially or fully replacing the bromide precursor with the corresponding iodide precursor, it is possible to synthesize mixed- and pure-halide $Cs_2TiBr_{6-x}I_x$ NCs, with a tunable bandgap between 1.2 eV and 2.3 eV. All the NCs show the expected cubic crystal structure, with the lattice parameter increasing from pure bromide to pure iodide. Moreover, we have observed that the method used to quench the reaction plays a fundamental role in determining the shape of the NCs, while the role of the zwitterionic ligand is important in stabilizing the nanoparticles during the washing step. Finally, the Cs_2TiBr_6 NC films decompose quickly in air, while they are stable for 1 hour at 100 °C and for 4 hours under UV light in a nitrogen atmosphere.

Experimental section

Chemicals

Cesium acetate (CsAc 99.9% trace metals basis), titanium(IV) isopropoxide (Ti(O-i-Pr)$_4$, ≥97.0%), oleic acid (OlAc, technical

grade 90%), bromotrimethylsilane (TMSBr, 97%), 3-(N,N-dimethyloctadecylammonio)propanesulfonate (≥99.0%) and acetone (≥99.5%) were purchased from Sigma-Aldrich. Iodotrimethylsilane (TMSI, 97%) was purchased from Fischer Scientific. Toluene (anhydrous, 99.8%) was purchased from Scharlabs. 1-Octadecene (90%) was purchased from Alfa Aesar. All chemicals were used without any further purification.

Preparation of titanium oleate solution

For the synthesis of titanium oleate, 16 ml of oleic acid was loaded in a 50 ml three-neck flask and degassed through 3 cycles of argon and vacuum treatment. 2 ml of titanium (IV) isopropoxide taken from the glovebox was slowly added while stirring and the solution was heated under argon for 1 hour at 140 °C. Afterwards, the solution was left under a vacuum at 110 °C overnight and acquired a dark red tone. The as-prepared solution was stored under nitrogen.

Synthesis of $Cs_2TiBr_{6-x}I_x$ nanocrystals

120 mg of cesium acetate (0.625 mmol) and 60 mg of 3-(N,N-dimethyloctadecylammonio)propanesulfonate were weighed in the glovebox and loaded in a 50 ml three-neck flask together with 2 ml of octadecene, 2 ml of oleic acid and 1.85 ml of titanium oleate solution (0.78 mmol). The solution was degassed through 3 cycles of argon and vacuum treatment and heated at 110 °C for 35 minutes under a vacuum. At this point, for the case of Cs_2TiBr_6 synthesis, 574 μl (4.218 mmol) of TMSBr was injected under argon at 140 °C and the reaction was carried out for 20 seconds and then quenched by diluting the solution with 15 ml of toluene. For the case of Cs_2TiI_6, 1238 μl (8.436 mmol) of TMSI was needed to prepare pure Cs_2TiI_6. For the mixed halide perovskite synthesis, different amounts of TMSBr and TMSI were mixed in the glovebox and injected in the flask, taking into account the optimal moles for the two pure halide perovskite syntheses. For instance, for the 70% synthesis, 70% of the iodide precursor used in the pure iodide perovskite synthesis was mixed with 30% of the bromide precursor used in the pure bromide perovskite synthesis. For the case of the Cs_2TiBr_6 and mixed-halide perovskite NC solutions, the washing procedure was carried out by adding 5 ml of acetone as an antisolvent to 5 ml of solution already diluted in

toluene and centrifuging at 5800 rpm for 10 minutes, while for the Cs_2TiI_6 NC solution no antisolvent was added before centrifuging. The supernatant was discarded and the precipitate redispersed in 1 ml of toluene and centrifuged again at 1000 rpm for 2 minutes to remove possible aggregates. The supernatant was filtered using a 0.22 μm PTFE filter. The solutions were stored in the fridge.

X-Ray diffraction (XRD) characterization

XRD patterns were collected using a Rigaku SmartLab diffractometer in a Bragg–Brentano $\theta/2\theta$ geometry, with Cu kα radiation (wavelength = 1.5406 Å) and a D/teX Ultra 250 silicon strip detector. The NC samples were prepared by drop casting the nanocrystal solutions on the top of a silicon wafer. All the samples were measured inside an air-sensitive sample holder, which was loaded in the glovebox to avoid any contact with air.

Transmission electron microscopy (TEM) characterization and elemental analysis

TEM measurements were performed at the Scientific and Technological Centres of the University of Barcelona (CCiT-UB). HRTEM images were acquired using a JEOL J2010F TEM microscope, equipped with a field emission electron gun (FEG). EDS experiments were carried out using a JEOL J2100 TEM microscope, equipped with a LaB_6 thermionic filament, and using an Oxford Instruments INCA X-sight spectrometer with a Si (Li) detector. Both microscopes were operated at an accelerating voltage of 200 kV. Samples for TEM characterization were prepared in the glovebox by drop-casting diluted toluene solutions (50 μl of NC solution in 1 ml of toluene) onto 200 mesh carbon-coated copper grids.

Elemental analysis of the samples was carried out using an inductively coupled plasma optical emission spectrometer (ICP-OES), PerkinElmer, model Optima 3200RL, in standard conditions.

UV-vis absorption and PL measurements

Optical absorption spectra were collected using a Varian Cary-5000 UV-vis-NIR spectrophotometer. Photoluminescence (PL) measurements were performed using a Horiba Jobin Yvon iHR550 Fluorolog system, with an OXXIUS 405 nm continuous wave laser as the source. The PL spectra were corrected for the system response function.

Conflicts of interest

There are no conflicts to declare.

Acknowledgements

References

1 A. Kojima, K. Teshima, Y. Shirai and T. Miyasaka, *J. Am. Chem. Soc.*, 2009, **131**, 6050–6051.

2 C. Wehrenfennig, M. Liu, H. J. Snaith, M. B. Johnston and L. M. Herz, *Energy Environ. Sci.*, 2014, **7**, 2269–2275.

3 G. Xing, N. Mathews, S. S. Lim, Y. M. Lam, S. Mhaisalkar and T. C. Sum, *Science*, 2013, **342**, 344–347.

4 R. E. Brandt, V. Stevanović, D. S. Ginley and T. Buonassisi, *MRS Commun.*, 2015, **5**, 265–275.

5 W. Meng, X. Wang, Z. Xiao, J. Wang, D. B. Mitzi and Y. Yan, *J. Phys. Chem. Lett.*, 2017, **8**, 2999–3007.

6 L. Protesescu, S. Yakunin, M. I. Bodnarchuk, F. Krieg, R. Caputo, C. H. Hendon, R. X. Yang, A. Walsh and M. V. Kovalenko, *Nano Lett.*, 2015, **15**, 3692–3696.

7 Q. Zhao, A. Hazarika, X. Chen, S. P. Harvey, B. W. Larson, G. R. Teeter, J. Liu, T. Song, C. Xiao, L. Shaw, M. Zhang, G. Li, M. C. Beard and J. M. Luther, *Nat. Commun.*, 2019, **10**, 1–8.

8 A. Hazarika, Q. Zhao, E. A. Gaulding, J. A. Christians, B. Dou, A. R. Marshall, T. Moot, J. J. Berry, J. C. Johnson and J. M. Luther, *ACS Nano*, 2018, **12**, 10327–10337.

9 Q. A. Akkerman, M. Gandini, F. Di Stasio, P. Rastogi, F. Palazon, G. Bertoni, J. M. Ball, M. Prato, A. Petrozza and L. Manna, *Nat. Energy*, 2016, **2**, 1–7.

10 S. T. Ochsenbein, F. Krieg, Y. Shynkarenko, G. Rainò and M. V. Kovalenko, *ACS Appl. Mater. Interfaces*, 2019, **11**, 21655–21660.

11 J. Li, L. Xu, T. Wang, J. Song, J. Chen, J. Xue, Y. Dong, B. Cai, Q. Shan, B. Han and H. Zeng, *Adv. Mater.*, 2017, **29**, 1603885.

12 D. H. Kwak, D. H. Lim, H. S. Ra, P. Ramasamy and J. S. Lee, *RSC Adv.*, 2016, **6**, 65252–65256.

13 S. Yakunin, L. Protesescu, F. Krieg, M. I. Bodnarchuk, G. Nedelcu, M. Humer, G. De Luca, M. Fiebig, W. Heiss and M. V. Kovalenko, *Nat. Commun.*, 2015, **6**, 1–9.

14 G. Flora, D. Gupta and A. Tiwari, *Interdiscip. Toxicol.*, 2012, **5**, 47–58.

15 M. R. Filip and F. Giustino, *J. Phys. Chem. C*, 2016, **120**, 166–173.

16 S. Khalfin and Y. Bekenstein, *Nanoscale*, 2019, **11**, 8665–8679.

17 F. Giustino and H. J. Snaith, *ACS Energy Lett.*, 2016, **1**, 1233–1240.

18 B. Saparov, J. P. Sun, W. Meng, Z. Xiao, H. S. Duan, O. Gunawan, D. Shin, I. G. Hill, Y. Yan and D. B. Mitzi, *Chem. Mater.*, 2016, **28**, 2315–2322.

19 A. Wang, X. Yan, M. Zhang, S. Sun, M. Yang, W. Shen, X. Pan, P. Wang and Z. Deng, *Chem. Mater.*, 2016, **28**, 8132–8140.

20 N. Sakai, A. A. Haghighirad, M. R. Filip, P. K. Nayak, S. Nayak, A. Ramadan, Z. Wang, F. Giustino and H. J. Snaith, *J. Am. Chem. Soc.*, 2017, **139**, 6030–6033.

11102 | *J. Mater. Chem. C*, 2021, **9**, 11098–11103

This journal is © The Royal Society of Chemistry 2021

21 I. Vázquez-Fernández, S. Mariotti, O. S. Hutter, M. Birkett, T. D. Veal, T. D. C. Hobson, L. J. Phillips, L. Danos, P. K. Nayak, H. J. Snaith, W. Xie, M. P. Sherburne, M. Asta and K. Durose, *Chem. Mater.*, 2020, **32**, 6676–6684.

22 A. Abfalterer, J. Shamsi, D. J. Kubicki, C. N. Savory, J. Xiao, G. Divitini, W. Li, S. Macpherson, K. Gałkowski, J. L. Macmanus-Driscoll, D. O. Scanlon and S. D. Stranks, *ACS Mater. Lett.*, 2020, **2**, 1644–1652.

23 M. G. Ju, M. Chen, Y. Zhou, H. F. Garces, J. Dai, L. Ma, N. P. Padture and X. C. Zeng, *ACS Energy Lett.*, 2018, **3**, 297–304.

24 M. Chen, M. G. Ju, A. D. Carl, Y. Zong, R. L. Grimm, J. Gu, X. C. Zeng, Y. Zhou and N. P. Padture, *Joule*, 2018, **2**, 558–570.

25 B. Lee, A. Krenselewski, S. Il Baik, D. N. Seidman and R. P. H. Chang, *Sustainable Energy Fuels*, 2017, **1**, 710–724.

26 X. Yang, Y. Chen, P. Liu, H. Xiang, W. Wang, R. Ran, W. Zhou and Z. Shao, *Adv. Funct. Mater.*, 2020, **30**, 1–8.

27 D. Kong, D. Cheng, X. Wang, K. Zhang, H. Wang, K. Liu, H. Li, X. Sheng and L. Yin, *J. Mater. Chem. C*, 2020, **8**, 1591–1597.

28 C. N. Savory, A. Walsh and D. O. Scanlon, *ACS Energy Lett.*, 2016, **1**, 949–955.

29 J. Euvrard, X. Wang, T. Li, Y. Yan and D. B. Mitzi, *J. Mater. Chem. A*, 2020, **8**, 4049–4054.

30 M. Antler and A. W. Laubengayer, *J. Am. Chem. Soc.*, 1955, **77**, 5250–5253.

31 F. Krieg, S. T. Ochsenbein, S. Yakunin, S. Ten Brinck, P. Aellen, A. Süess, B. Clerc, D. Guggisberg, O. Nazarenko, Y. Shynkarenko, S. Kumar, C. J. Shih, I. Infante and M. V. Kovalenko, *ACS Energy Lett.*, 2018, **3**, 641–646.

32 J. L. Mendes, W. Gao, J. L. Martin, A. D. Carl, N. A. Deskins, S. Granados-Focil and R. L. Grimm, *J. Phys. Chem. C*, 2020, **124**, 24289–24297.

This journal is © The Royal Society of Chemistry 2021

J. Mater. Chem. C, 2021, **9**, 11098–11103 | **11103**